



Bi metal sphere/graphene oxide nanohybrids with enhanced direct plasmonic photocatalysis

Zhenyu Wang^a, Shuai Yan^b, Yanjuan Sun^a, Ting Xiong^a, Fan Dong^{a,*}, Wei Zhang^{c,*}

^a Chongqing Key Laboratory of Catalysis and New Environmental Materials, College of Environment and Resources, Chongqing Technology and Business University, Chongqing, 400067, China

^b Institute of Microelectronics, Chinese Academy of Sciences, Beijing 100029, China

^c Chongqing Institute of Green and Intelligent Technology, Chinese Academy of Sciences, Chongqing 400714, China

ARTICLE INFO

Article history:

Received 13 February 2017

Received in revised form 8 May 2017

Accepted 12 May 2017

Available online 15 May 2017

Keywords:

Bi metal sphere

Graphene oxide

Nanohybrids

Direct plasmonic photocatalysis

Mechanism

ABSTRACT

The Bi metal sphere/graphene oxide (Bi/GO) nanohybrids were firstly synthesized by a simple one-step solvothermal method. Compared with bare Bi spheres, the Bi/GO nanohybrids exhibited highly enhanced and stable direct plasmonic photocatalytic activity towards removal of NO, primarily resulting from the assistance of graphene oxide. The Bi spheres act as antenna for incident light absorption via the SPR effect. The graphene oxide is regarded as an acceptor and transporter of the photogenerated electrons and provides the binding sites for Bi deposition. Furthermore, the related growth and plasmonic photocatalytic mechanisms of Bi/GO nanohybrids system were proposed reasonably. The agreements of the simulation results and experimental study where Bi spheres and Bi/GO nanohybrids were applied as direct plasmonic photocatalysts were discussed for the first time. This work could not only provide new insights into the understanding of the plasmonic effects of Bi spheres but also pave a new way to design direct plasmonic photocatalysts with superior performance.

© 2017 Elsevier B.V. All rights reserved.

1. Introduction

Graphene oxide (GO) is constituted structurally of hydrophilic oxygenated graphene framework bearing oxygen-containing functional groups on their basal planes and edges [1]. Noticeably, the ionizable functional groups on GO act as binding sites that facilitate the deposition and anchoring of semiconductor, metal nanoparticles and organic (dye) molecules through direct noncovalent, covalent, $\pi-\pi$, and/or van der Waals interactions [2–4]. Furthermore, GO is an excellent electron acceptor and transporter which can facilitates the charge separation and migration to counteract electron-hole pair recombination rate effectively [5,6]. The fabrication of hybrid materials with the incorporation of oxidized graphene, especially graphene oxide/semiconductor composites, have been pursued intensively in recent years because of their promising sustainable applications in environmental conservation, catalysis, H₂ generation and light-energy harvesting [7–12].

The localized surface plasmon resonance (LSPR) effect is a collective oscillation of conduction electrons in metallic nanoparticles.

Recently, the localized surface plasmon resonance (LSPR) effect of nanoparticles such as gold (Au), silver (Ag), and copper (Cu) have been successfully applied to enhance the photocatalysis of semiconductors under visible light irradiation [13–15]. Similar to aforementioned metal nanoparticles, the semimetal bismuth, as a direct plasmonic photocatalyst, with unique electronic properties due to its small electron effective mass, large mean free path and low charge carrier density in the bulk form, has been found to exhibit stable plasmonic photocatalytic activity due to the SPR property [16–18]. However, the photocatalysis efficiency of Bi metal alone is unsatisfactory and needs to be further enhanced.

Despite manifold studies on various Bi nanostructures (nanorods, nanowires, nanotubes, nanoplates and nanospheres) [19,20], bismuth based oxides (Bi₂O₃, Bi₂O₂CO₃, BiOI, BiVO₄, Bi₂WO₆, Bi₂MoO₆, BiFeO₃, and Bi₂Ti₂O₇ [21–25], etc) and their composites (Bi₂O₃/CeO₂, BiOI/BiOCl, Bi₂O₃/Bi₂WO₆, BiVO₄/Co₃O₄, Ag₃PO₄/Bi₂MoO₆, BiFeO₃/PbO₃, Bi₂Ti₂O₇/TiO₂ [26–29], etc), the possibility of using elemental bismuth-based nanocomposites, especially Bi/GO as photocatalysts, and their related growth and photocatalytic mechanisms have not been explored. Meanwhile, few works have referred to the theoretical and numerical simulation of the plasmonic behavior of Bi and even fewer works have linked the theoretical study to experimental study.

* Corresponding authors.

E-mail addresses: dfctbu@126.com (F. Dong), andyzhangwei@163.com (W. Zhang).

Herein, we report a simple one-step solvothermal method to synthesize Bi metal spheres/graphene oxide (Bi/GO) nanohybrids and provide a simulation study of the optical responses, absorption efficiency and local electromagnetic field over Bi spheres. Beyond the Bi spheres, the as-prepared Bi/GO nanohybrid, exhibited highly enhanced and stable photocatalytic activity towards removal of NO under 280 nm light irradiation, which can be ascribed to the assistance of GO. Semimetal bismuth, as a direct plasmonic photocatalyst, acts as antenna for incident light utilization. The photocatalytic efficiency of Bi/GO is greatly enhanced due to the pivotal roles of GO in three aspects: (i) acting as an acceptor and transporter of the photogenerated electrons from the surface plasmon resonance (SPR) of Bi, (ii) providing binding sites that facilitate the deposition and anchoring of Bi and yielding intimate contact between Bi and GO, and (iii) enhancing the NO adsorption of hybrid and increasing pollutant concentration in the active sites. Also, in contrast to the pure Bi spheres, the Bi spheres in the Bi/GO composite yield strong electromagnetic field to accelerate charge transfer due to the proper diameter. In addition, the growth mechanism of Bi/GO nanohybrid was discussed, which was associated with the Ostwald ripening.

2. Experimental section

2.1. Synthesis of Bi spheres/GO and bare Bi spheres

All chemicals used in this study were analytical grade (Sigma Aldrich) and were used without further purification. The Bi/GO nanohybrids were synthesized by one-step solvothermal method. In a typical synthesis, 0.364 g $\text{Bi}(\text{NO}_3)_3 \cdot 5\text{H}_2\text{O}$ was dissolved in HNO_3 solution (10 mL, 1 M), followed by the addition of 55 mL ethylene glycol containing well-dispersed graphene oxide (0.0078 g, 5 wt.%), and stirred vigorously for 30 min. 0.6 g of poly-vinylpyrrolidone (PVP) were dissolved with stirring in the above mixture. Then the mixture was put into a 100 mL stainless steel autoclave with Teflon liner at 160 °C for 12 h. The products were recovered by filtration, rinsed by deionized water and ethanol for three times, and then dried at 60 °C for 12 h. For comparison, bare Bi nanospheres were prepared using the same hydrothermal method without the addition of GO.

2.2. Characterization

The crystal phases of the sample were analyzed by X-ray diffraction (XRD) with $\text{Cu K}\alpha$ radiation (model D/max RA, Rigaku Co., Japan). X-ray photoelectron spectroscopy (XPS) with $\text{Al K}\alpha$ X-rays ($\text{h}\nu = 1486.6 \text{ eV}$) radiation and Ar electronic gun (2 keV) to etch sample surface for 30 s (Thermo ESCALAB 250, USA) was used to investigate the surface properties. Scanning electron microscopy (SEM, model JSM-6490, JEOL, Japan) and transmission electron microscopy (TEM: JEM-2010, Japan) were used to characterize the morphology of the obtained products. The UV-vis diffuse reflectance spectrometry (DRS) spectra were obtained for the dry-pressed disk samples using a Scan UV-vis spectrophotometer (TU-1901, China) equipped with an integrating sphere assembly, using BaSO_4 as the reflectance sample. The sample for electron spin resonance (ESR) measurement was prepared by mixing the as-prepared samples in a 50 mM DMPO solution tank (methanol dispersion for DMPO-O_2^- and aqueous dispersion for DMPO-OH) under irradiation with 280 nm light. To determine the involvement of active species during photocatalysis, we performed trapping experiments for the detection of holes and electrons. The scavengers used in this research are potassium iodide (KI, 1 wt.%) for holes, potassium dichromate ($\text{K}_2\text{Cr}_2\text{O}_7$, 1 wt.%) for electrons. Photoelectrochemical properties of the as-prepared samples were

evaluated using a CH 660D electrochemical workstation in a conventional three-electrode cell, with a Saturated calomel electrodes and as-prepared samples film electrodes on ITO as the reference electrode and working electrodes, respectively. The photocurrent-time curves were measured at open circuit potential in 0.5 mol/L Na_2SO_4 at ambient temperature under a 280 nm UV lamp.

2.3. Simulation of absorption efficiency and electromagnetic field distribution of spherical Bi particles with different sizes

In order to further depict the localized surface plasmonic resonance (LSPR) with different size, the optical spectra of bismuth nanospheres are simulated both with Mie theory (MT) and a finite integration technique (FIT) [30]. The dielectric function of Bi is fitted to Drude model by a least square procedure. The computational domain is a cubic volume whose edge length is set to 4 times the diameter of the particles. The spherical particle is placed in the center of the cubic. The perfect matched Layer (PML) absorbing boundary condition is applied around the volume. The computational domain is discretized by a structured mesh. A frequency domain simulation is then carried out by our FIT code. The simulation of the field distribution at and around the Bi nanospheres is carried out with a rigorous Maxwell's solver based on the finite integration techniques. A time-harmonic inverse iterative method (THIIM) is utilized to overcome the instability problem caused by the negative permittivity of the metal [31]. The implementation of the method is parallelized to deal with the large number of degrees of freedom needed for the simulation of multiscale structures involving plasmonic effects [32]. The computational domain is a sphere with the Bi particle placed in the center, and the surrounding is the free space. A perfect matched layer is applied to all the sides to truncate the computational region. The refractive index of Bi in the UV to the near-infrared spectrum is obtained by a fit to the Drude model of the empirical data [33].

2.4. Evaluation of photocatalytic activity

The photocatalytic activity was tested by the removal of NO at ppb levels in a continuous flow reactor at ambient temperature. The volume of the rectangular reactor, made of stainless steel and covered with Saint-Glass, was 4.5 L (30 cm × 15 cm × 10 cm). For activity test under 280 nm and 360 nm, UV lamps (8 W and 6 W) were vertically placed outside the reactor, respectively. For the visible light photocatalytic activity test, a 150 W commercial tungsten halogen lamp was used, and a UV cut off filter (420 nm) was adopted to remove UV light in the light beam. 0.20 g of the as-prepared sample was dispersed in distilled water (60 mL) in a beaker via ultrasonic treatment for 10 min and then coated onto two glass dishes (12.0 cm in diameter). These dishes were then pretreated at 60 °C to remove the water in the suspension and cooled to room temperature before the photocatalytic test.

The NO gas was acquired from a compressed gas cylinder at a concentration of 100 ppm of NO (N_2 balance). The initial concentration of NO was diluted to about 660 ppb by the air stream supplied by compressed standard air. The relative humidity in the present system is controlled at 50% to simulate the indoor environmental conditions by passing the zero air streams through a humidifier in the gas flow. The gas streams were premixed completely by a gas blender, and the flow rate of the air stream and NO were controlled at $2.4 \text{ L} \cdot \text{min}^{-1}$ and $15 \text{ mL} \cdot \text{min}^{-1}$, respectively, by a mass flow controller. After the adsorption-desorption equilibrium was achieved in the dark, the lamp was turned on. The concentration of NO was continuously measured by a chemiluminescence NO analyzer (model 42i-TL, Thermo Environmental Instruments Inc), which monitors NO, NO_2 , and NO_x (NO_x represents $\text{NO} + \text{NO}_2$) with a sampling rate of 0.7 L/min. The removal ratio (η) of NO was calcu-

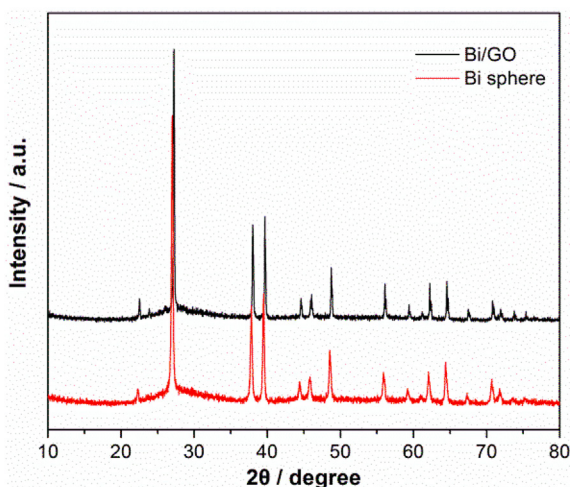


Fig. 1. XRD patterns of the as-synthesized Bi spheres and Bi/GO hybrids.

lated as $\eta(\%) = (1 - C/C_0) \times 100\%$, where C and C_0 are concentrations of NO in the outlet and feeding stream, respectively.

3. Results and discussions

3.1. Structure and morphology

The crystallographic structures of Bi spheres and Bi/GO hybrids were characterized by XRD, as shown in Fig. 1. The XRD pattern of the as-synthesized Bi spheres is well indexed as rhombohedral Bi metal (JCPDS card no. 05-0519), and no other impurity peak is observed. Similar XRD peaks of rhombohedral Bi are detected for the Bi/GO composite. The absence of GO phase diffraction peaks may be due to the low content and weak diffracted intensity. It is noted that no obvious chemical shift of the diffraction peaks of Bi are observed in the Bi/GO composite when compared with that of pure Bi sphere, indicating that the structure of Bi in the composite are well maintained [34].

The detailed morphology of the bare Bi spheres and Bi/GO hybrids were characterized by scanning electron microscopy (SEM). For pure Bi spheres, a large number of Bi spheres with an average diameter of 300 nm (Fig. 2a) can be observed. The surface of Bi spheres consists of numerous interconnected small nanoparticles (Fig. 2b). Fig. 2c also confirms its spheres structure composed of small nanoparticles. The high-resolution transmission electron microscopy (HRTEM) image shows a lattice fringe of 0.19 nm, corresponding to the (021) crystal facet of rhombohedral Bi metal (Fig. 2d).

For the Bi/GO hybrids, as can be observed in Fig. 3a, the Bi spheres are *in situ* grew on the layered structure of the GO substrates. The GO substrate presents a higher density of oxygen functionalities at its surface which may promote the dispersion of the Bi spheres. Furthermore, in the presence of GO, compared with pure Bi spheres system, the average diameter of the Bi nanospheres decrease to about 200 nm (Fig. 3b). As noticed previously, the coordinative bonding of PVP plays a critical role in size control of metal nanoparticles [35,36]. The Bi^{3+} -PVP concentration decreases due to the adsorption of the Bi^{3+} ions by the oxygen functional groups of GO via electrostatic interactions and the nonbonding PVP concentration increases accordingly, both of which could decrease the size of Bi nanospheres.

The TEM image (Fig. 3c) further reveals that the synthesized Bi shperes are *in situ* loaded on the surface of graphene oxide nanosheets. Fig. 3d exhibits the HRTEM image of Bi/GO hybrid. The boundary of Bi sphere and GO can be observed. The spacing

of 0.328 nm corresponds to the (012) plane of rhombohedral Bi surrounded by amorphous GO layers. Obviously, intimate contact between Bi nanosphere and GO can be achieved, which could effectively promote the transfer of photogenerated carriers between the two components.

The EDS mapping images (Fig. S1) indicate that the Bi/GO hybrids contain Bi, C and O elements, suggesting the co-existence of bismuth and grapheme oxide. In Fig. S1c, the widely dispersed O element, attributing to higher density of oxygen functionalities of GO substrate, can be observed. The corresponding BET surface areas and porous structures of the two samples were investigated using nitrogen adsorption-desorption experiments (Fig. S2). The BET surface areas of the Bi and Bi/GO hybrid are determined to be 16.2 and $13.6 \text{ m}^2 \text{ g}^{-1}$, respectively. The addition of GO slightly decreases the BET surface areas. The isotherms of the two samples were characteristic of type IV with a hysteresis loop, implying their mesoporous structure (Fig. S2a) [37]. The pore-size distributions in Fig. S2b indicate a pore-size distribution around 4 nm and in the range of 10–100 nm, confirming the presence of a large number of mesopores and macropores, consistent with their morphology.

3.2. Growth mechanism of bare Bi spheres and Bi spheres/GO

On the basis of the above observations, the related growth mechanism of Bi spheres was proposed in Fig. S3 and Fig. 4a. In the initial stage, the coordinative bonding is formed between the carbonyl oxygen of PVP and bismuth ion (Bi^{3+} -PVP). During the solvothermal process, the tiny Bi crystal particles were formed via reducing of Bi^{3+} by EG, producing bismuth adatoms (Bi-PVP) protected by PVP. The subsequent step is that the PVP could accelerate the formation of a large amount of bismuth nuclei clusters and prohibit the grain growth and particle aggregation (Fig. S3). Then, the PVP, as a capping agent, is coating on the surface of Bi particles and the free PVP wrapping the Bi-PVP complexes to generate sphere-like micelles in the EG solvent, leading to the formation of sphere assembled by numerous interconnected nanoparticles through the process known as Ostwald ripening (Fig. 4a).

The growth mechanism for the formation of Bi sphere/GO is schematically illustrated in Figs. 4 b and 5 . GO sheets bear bulky hydroxyl and epoxy functional groups on their basal planes in addition to carbonyl and carboxyl groups located at the sheet edges. These functional groups provide reactive sites for the bismuth nuclei clusters and govern the nucleation of nanoparticles. From the chemical point of view, it is supposed that the overall oxygen functional groups can be used as anchors for adsorption of the Bi^{3+} ions in solution because of electrostatic interactions (Fig. 5). Afterward, the addition of the reducing agent (EG) and stabilizer (PVP) to the precursor solution promote the subsequent *in situ* reduction of Bi^{3+} ions and formation of Bi nanoparticles, enabling the growth of Bi spheres on the GO surface (Figs. 4 b and 5). In order to investigate the role of PVP during the processes of Bi spheres formation, the Bi sample was synthesized in absence of PVP and the SEM images were shown in Fig. S4. Obviously, Bi nanosphere structure cannot be generated. Instead, without PVP addition, the random bulk structure (Fig. S4a) with size distribution at 5–30 nm (Fig. S4b) is produced, which means PVP plays a crucial role in nanosphere morphology formation. So, preparation of Bi-GO with EG and PVP can readily control the shape, size, and distribution of spheres and their interfacial characteristics via the *in situ* growth, attributing to the electrostatic interaction between the Bi^{3+} and the oxygen functional groups of GO.

3.3. Chemical composition

To investigate the chemical composition of the catalysts, the XPS spectra of Bi/GO nanohybrids before and after ion etching are com-

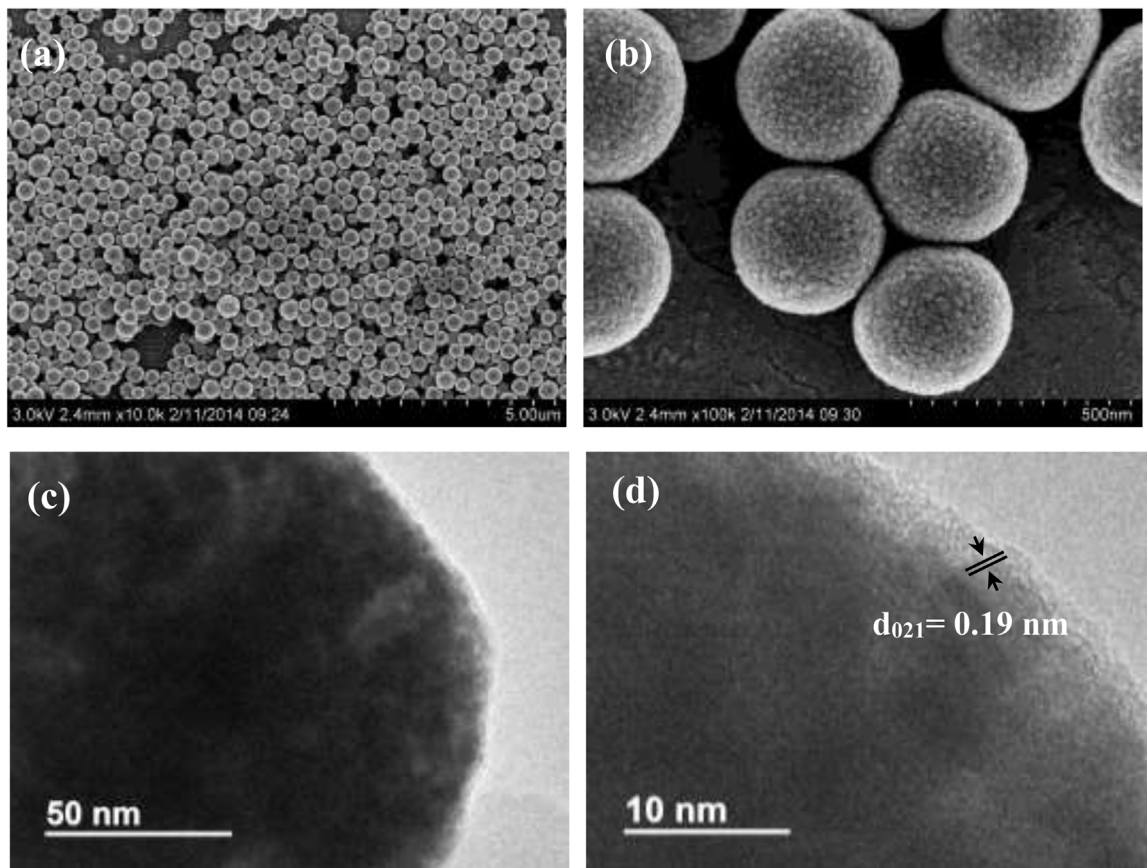


Fig. 2. SEM images (a, b), TEM image (c) and HRTEM image (d) of pure Bi spheres.

pared. The Bi 4f XPS spectra show the considerable differences after etching (Fig. 6a). The peaks at 159.4 and 164.7 eV are the characteristic of Bi ions in bismuth oxide, and no prominent peaks of Bi–Bi bonds can be observed simultaneously, which can be attributed to the oxygen rich surface of the original Bi spheres [16]. After ion etching, the typical Bi–Bi bonds of elemental Bi peaks centered around 157.2 and 162.5 eV can be detected and the peak intensity of Bi–O bond decrease. This result further demonstrates that the oxide layer exclusively exists on the Bi sphere surface, which could prevent the Bi metal from further oxidation [16]. The C 1s spectra of Bi/GO composite could be fitted into three peaks at 284.8, 286.4 and 288.2 eV, which are associated with sp^2 -hybridized carbon (C=C), hydroxyl carbon (C–O), and carboxyl carbon (O=C–O) of GO, respectively [38,39]. Nevertheless, after ions etching, the amount of oxygen-containing groups (C–O, O=C–O) are remarkably reduced as shown in Fig. 6b. In addition, the O 1s peak (Fig. S5) before etching shows marked characteristic of oxygen species at binding energies of around 529.9, 531.4 and 532.6 eV, arising from the Bi–O, C–O and O–H bonds, respectively. After ions etching, these three peaks are decreased. The decrease of C 1s and O 1s spectra after etching confirms the structure of Bi spheres attached on the GO substrates. XPS, SEM and TEM results confirm the successful synthesis of Bi/GO nanohybrids with intimate contact and strong interaction.

3.4. Optical properties

UV-vis DRS was used to investigate the optical properties of Bi sphere and Bi/GO nanohybrids. In Fig. 7a, both of the samples show strong and broad absorption peak at ca. 260 nm in the ultra-violet and weak absorption in the visible range between 400 and

550 nm, which indicates the SPR property in near ultra-violet and visible range when the particle size of Bi is larger than 100 nm. The enlarged view of absorption range between 200 and 400 nm in Fig. 7b shows that the resonance peak is blue shifted as the average diameter of Bi sphere in Bi/GO nanohybrids (ca. 200 nm) is smaller than pure Bi sphere (ca. 300 nm).

In order to further depict the localized surface plasmonic resonance (LSPR) with different sizes, the optical spectra of bismuth spheres are simulated both with Mie theory (MT) and a finite integration technique (FIT). The dielectric function of Bi is fitted to Drude model by a least square procedure. Due to the oxide layer existing on the as-obtained Bi nanosphere surface, it is more difficult to obtain the optical constants of Bi experimentally. Therefore, we take the empirical values and fit them to the analytical Drude model (Eq. (1)) for the evaluation of the optical spectra which could fit the empirical data from 200 to 800 nm [33]. We do not take any Lorenz oscillator terms for a balance between accuracy of the model and the fit.

$$\epsilon_D(\omega) = \epsilon_D(\infty) - \frac{\omega_D^2}{\omega^2 + i\Gamma_D\omega} \quad (1)$$

Using Mie theory, we compare the optical responses of spherical Bi particles and the absorption efficiency of particles of 50–300 nm diameters is plotted in Fig. 7c. As the diameter of the Bi particle decreases, the absorption peak induced by the SPR is blue-shifted. Besides, the absorption spectrum based on the FIT code is simulated as shown in Fig. 7d, and the absorption here is defined as the proportion of the absorbed power in the total incident power. Obviously, these absorption spectra could fit well with the Mie calculation results. From the above results, it can be concluded that the simulation results agree with the experimental study. Both experimental

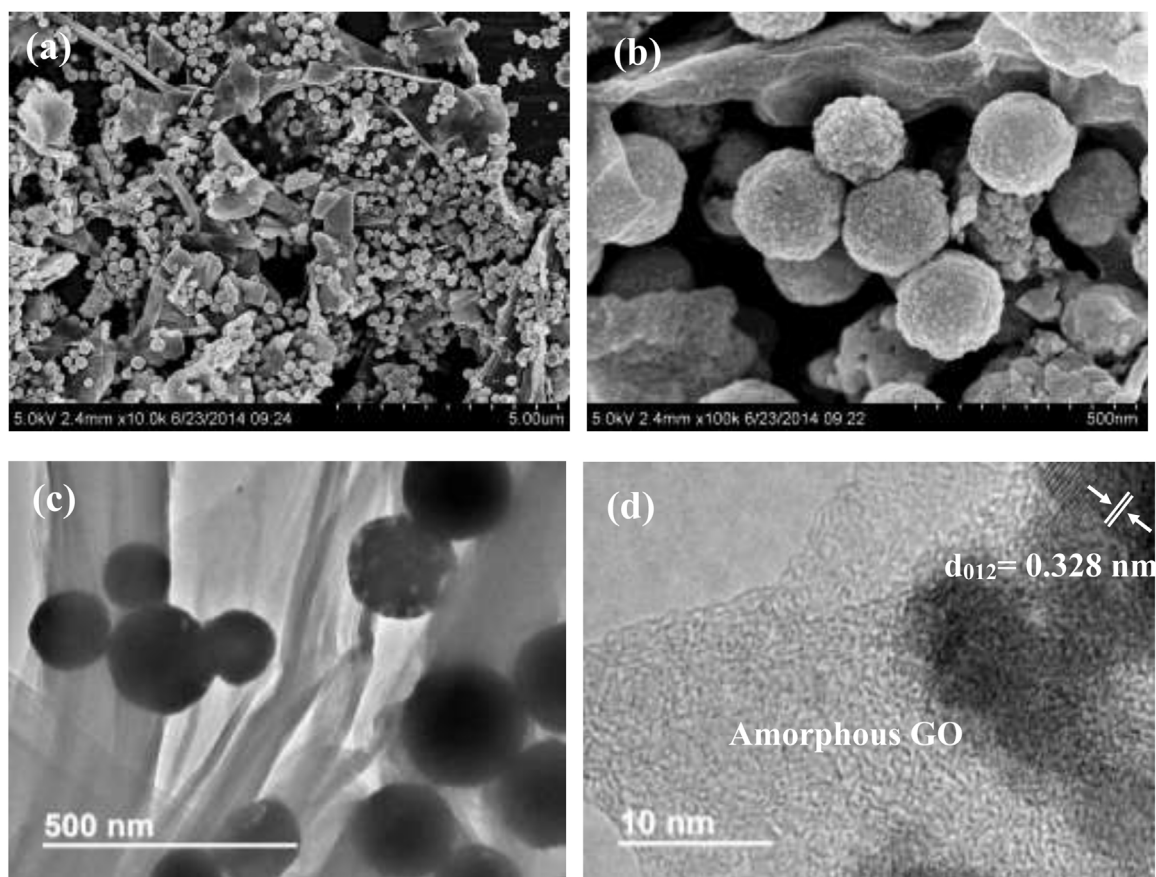


Fig. 3. SEM images (a, b), TEM image (c) and HRTEM image (d) of Bi/GO hybrid.

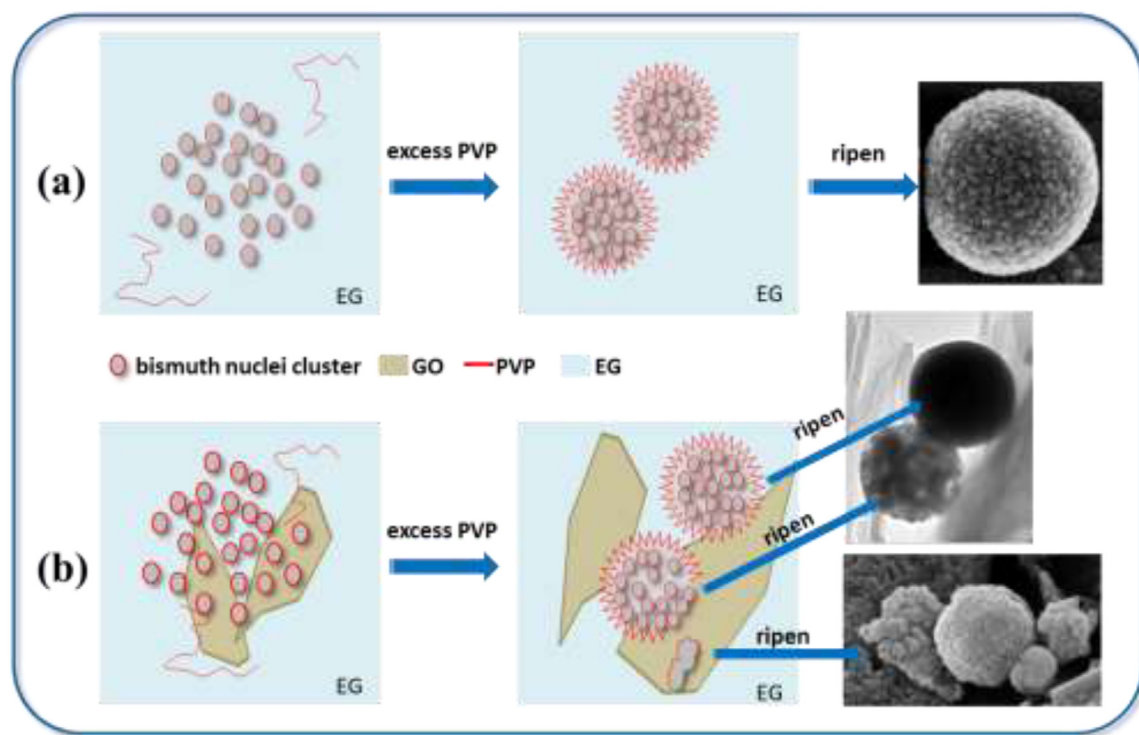


Fig. 4. Proposed schemes for the fabrication of the Bi sphere (a), Bi sphere/GO nanohybrids (b).

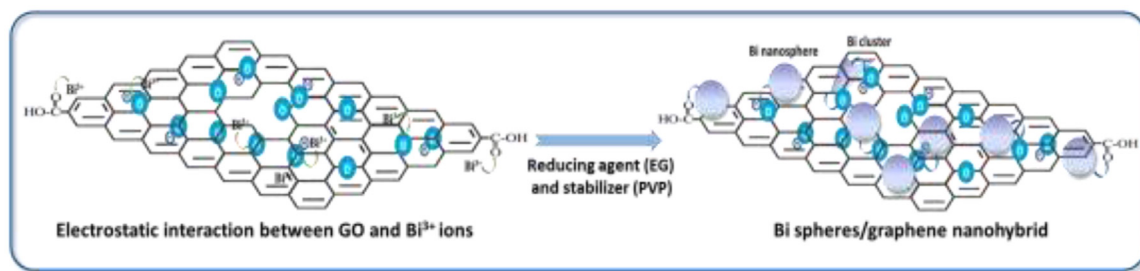


Fig. 5. Schematic representation of the mechanism of nucleation of bismuth spheres on the GO surface.

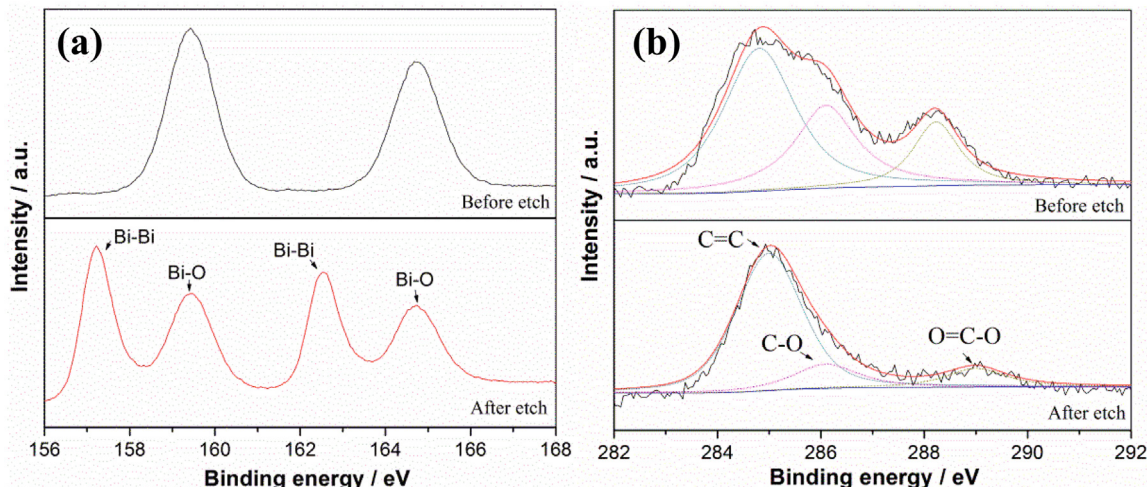


Fig. 6. The Bi 4f (a) and C 1s (b) XPS spectra of Bi/GO nanohybrids before and after ion etching.

and simulation results demonstrate the LSPR of spherical Bi particles. Moreover, SPR peak is blue shifted because of the decreased diameter of the Bi spheres.

Here, the local electromagnetic field arising from the SPR effects of Bi nanospheres was simulated with a rigorous Maxwell's solver based on the finite integration techniques as shown in Fig. 8. A significant enhancement of electromagnetic field under UV light irradiation can be observed. The electromagnetic field reaches its maximum value in close proximity to the Bi nanosphere surface because of the SPR effect. Also, the intensity of the electromagnetic field first strengthens and then weakens with the increasing diameter of Bi nanosphere. Obviously, Bi nanospheres with diameter of 200 yield stronger electromagnetic field than that of Bi nanosphere with diameter of 300. It is expected that the Bi spheres in the Bi/GO nanohybrids would show stronger SPR effects than the pure Bi spheres. These calculation results indicate that the optical responses and surface plasmon resonance effects can be tuned by controlling the size of the Bi nanospheres, providing a powerful reference for future works about size-controlled SPR effect of Bi metal.

3.5. Plasmonic photocatalytic activity and stability in NO removal

The photocatalytic activity of Bi/GO composite and bare Bi spheres was evaluated towards removal of NO under light irradiation. Fig. 9a shows the variation of NO concentration ($C/C_0\%$) with irradiation time over samples. Here, C_0 and C are the concentration of NO at time zero and t , respectively. The NO adsorption equilibrium process of Bi/GO (as an example) before the light turned on is shown in Fig. S6. When the concentration of NO sustained stably for 5 min in the continuous flow reactor, the adsorption equilibrium control was finished and the light was turned on. Under UV

light (280 nm) irradiation, the NO concentration decreases rapidly through photocatalytic oxidation within the first 6 min. The final NO removal ratios of Bi/GO nanohybrids and pure Bi sphere are 50.2 and 36.9%, respectively. Obviously, the Bi/GO shows enhanced activity compared with that of pure Bi sphere although the Bi/GO has lower surface areas. The negligible photocatalytic activities of bare Bi spheres under 420 and 360 nm light irradiation can be observed, which indicates that the absorption at these wavelengths is inefficient to initiate photocatalysis [14]. According to the previous work, Bi displays SPR property in visible light range and electrons and holes are generated veritably under visible light illumination [14]. But the potential of electrons or holes are not negative or positive enough to induce the production of $\bullet\text{O}_2^-$ or $\bullet\text{OH}$ and the photon absorption is insufficient to break the N–O bond, leading to the poor photocatalytic activity in visible light region [14]. In addition, it is noteworthy that the Bi/GO nanohybrids did not reveal any reduction of their photocatalytic activity under UV light irradiation after 5 cycles (Fig. 9b), indicating their excellent photochemical stability.

The Bi/GO sample after cycling runs is collected and analyzed by XRD and TEM (Fig. S7). It is obvious that all diffraction peaks and morphology of the used Bi/GO sample are exactly identical to that of the fresh sample (Fig. 1 and Fig. 3c), both of which imply that the Bi/GO is stable in structure.

3.6. Mechanism of enhanced plasmonic photocatalysis with Bi/GO nanohybrids

To reveal the roles of the active species on the NO removal over the Bi/GO nanohybrids, the DMPO spin-trapping ESR spectra were performed. As shown in Fig. 10a and 10b, the characteristic peaks of DMPO- $\bullet\text{O}_2^-$ and DMPO- $\bullet\text{OH}$ can be observed under 280 nm UV

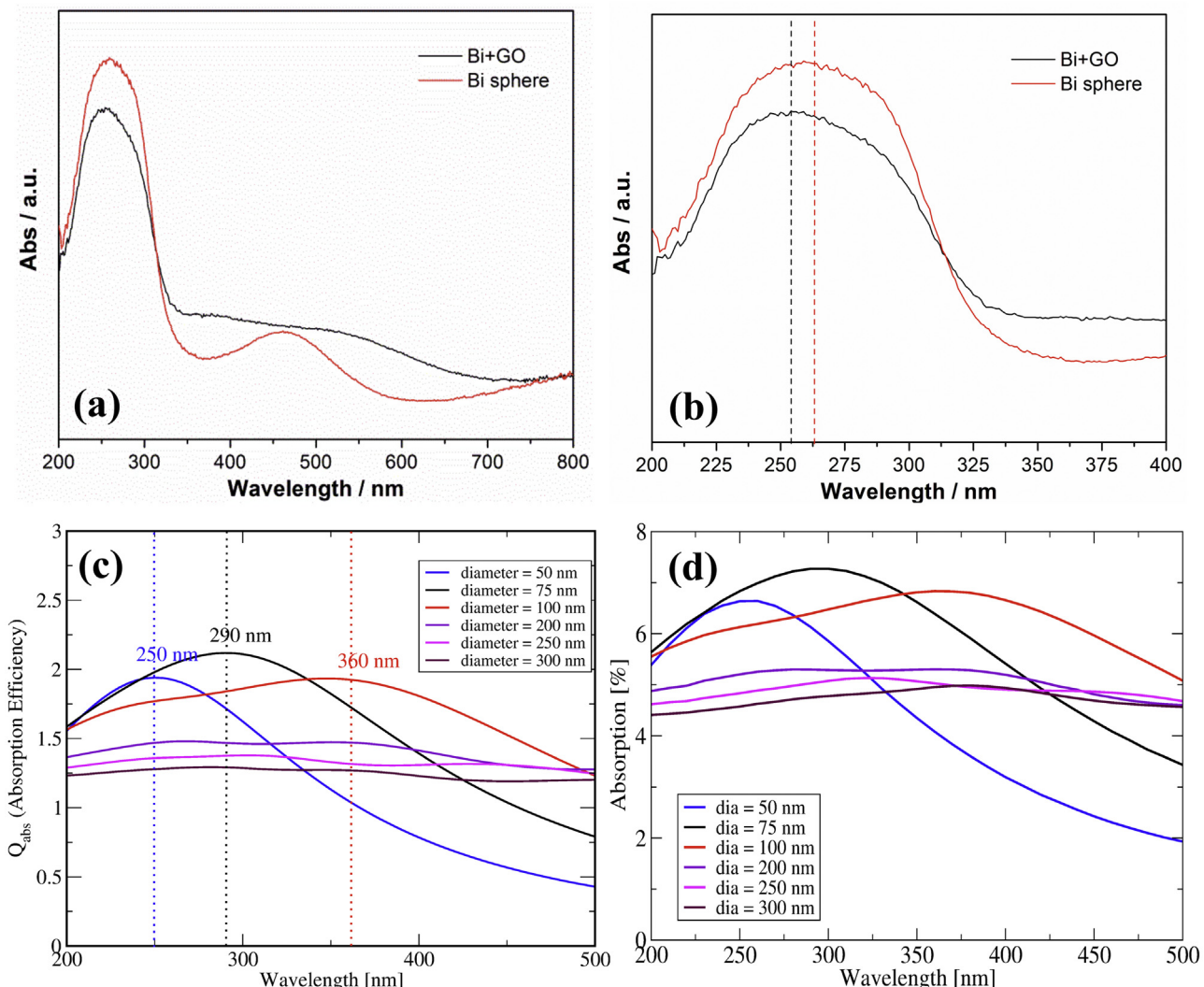


Fig. 7. UV-vis DRS of Bi sphere and Bi/GO samples (a, b), the absorption efficiency of spherical Bi particles with different sizes calculated by Mie Theory (c) and FIT (d).

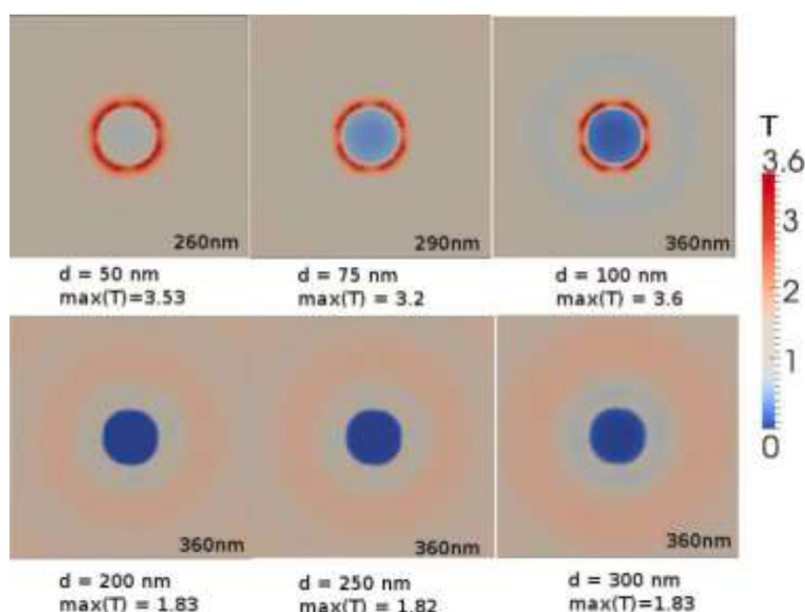


Fig. 8. The distribution of electromagnetic field about Bi nanospheres with different sizes.

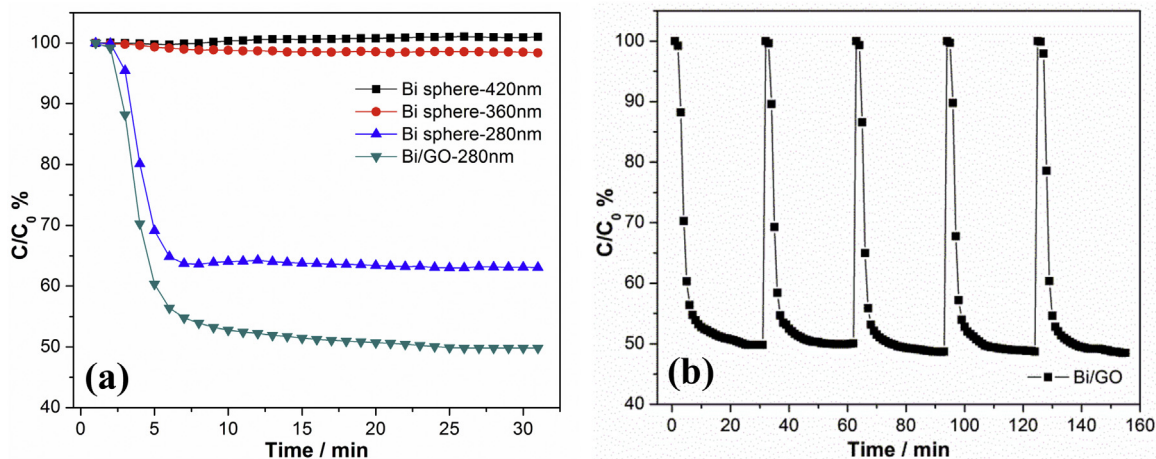


Fig. 9. photocatalytic activities of the bare Bi spheres and Bi/GO nanohybrids for removal of NO in air (a), and cycling runs for the photocatalytic removal of NO over Bi/GO nanohybrids under 280 nm (b).

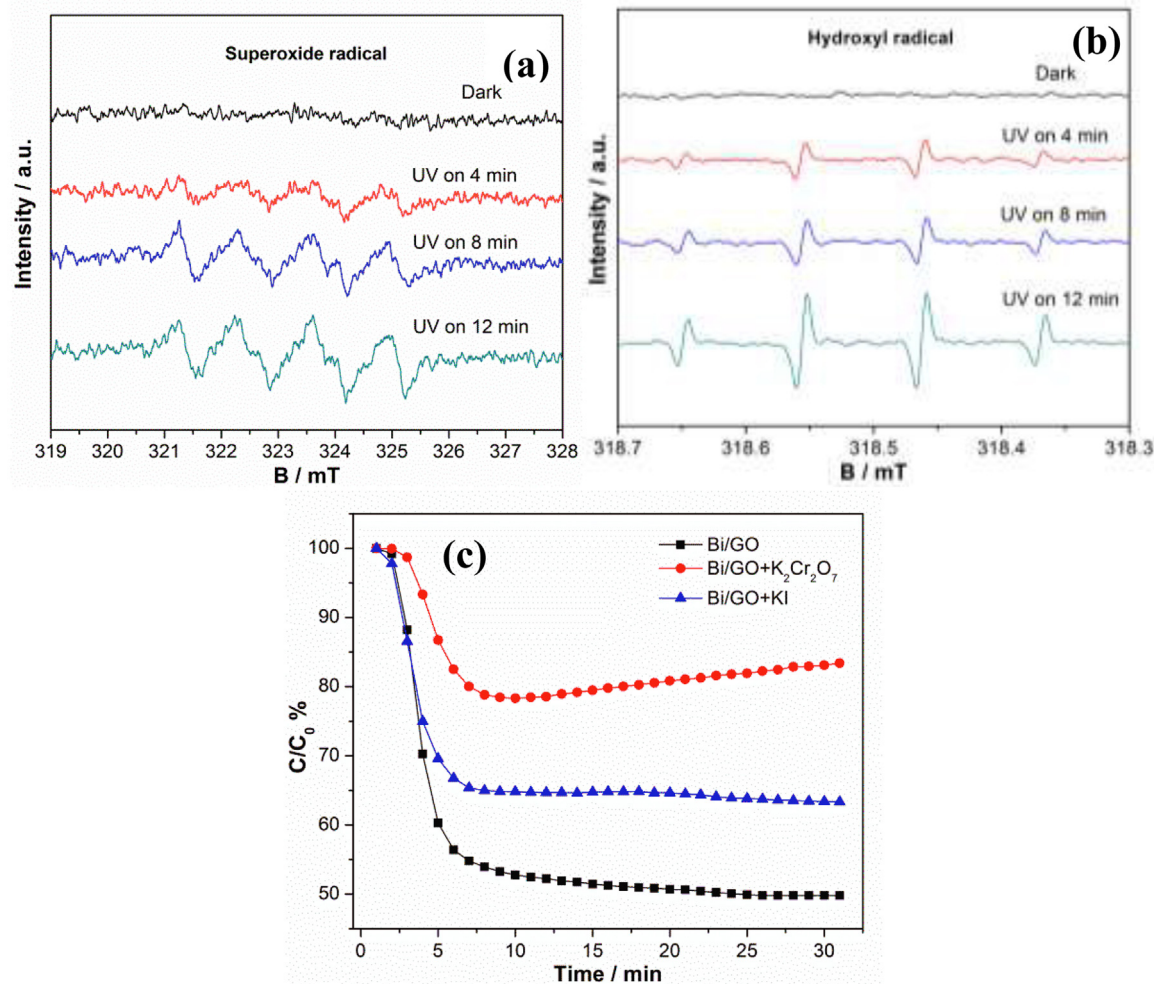


Fig. 10. DMPO spin-trapping ESR spectra of Bi/GO nanohybrids in methanol dispersion for DMPO-•O₂⁻ (a) and in aqueous dispersion for DMPO-•OH (b) and active species trapping experimental (c).

light illumination, indicating the production of $\cdot\text{O}_2^-$ and $\cdot\text{OH}$. To estimate the role of e^- and h^+ on NO removal during the irradiation period, active species trapping experimental was carried out (Fig. 10c). $\text{K}_2\text{Cr}_2\text{O}_7$ and KI serve as electron and hole scavengers, respectively [40]. It's worth noting that the addition of $\text{K}_2\text{Cr}_2\text{O}_7$

could inhibit 83.4% of NO removal, while the inhibition efficiency by KI is 63.3%. These results imply that the removal of NOx could be mainly attributed to the $\cdot\text{O}_2^-$ from the reduction of O_2 with electrons and the $\cdot\text{OH}$ from the oxidation H_2O with h^+ during the photocatalysis.

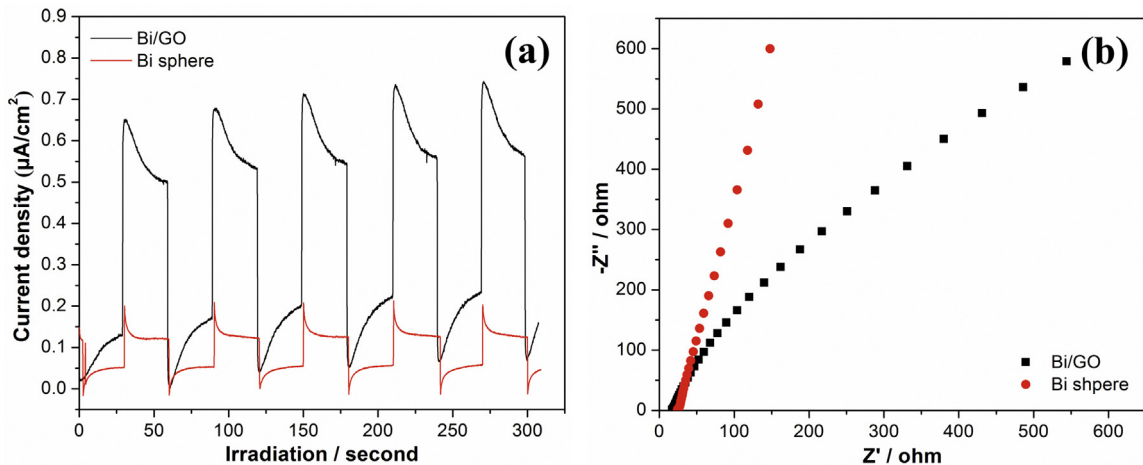


Fig. 11. Photocurrent transient (a) and Nyquist plots (b) for Bi/GO and bare Bi sphere electrodes under 280 nm UV light irradiation.

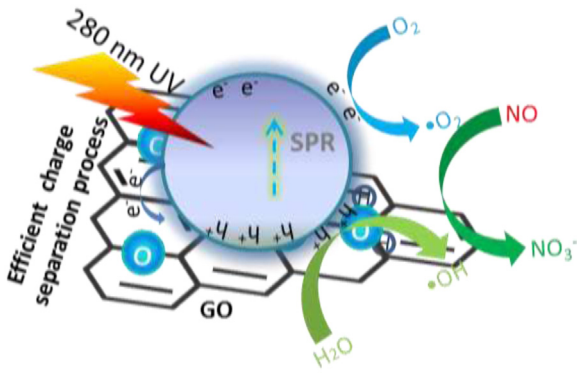
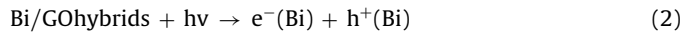


Fig. 12. Proposed mechanism for photocatalytic NO removal by Bi sphere/GO nanohybrids.

The photocurrent and electrochemical impedance spectra of the bare Bi spheres and Bi/GO nanohybrids were used to reveal the charge separation and transfer. As shown in Fig. 11a, the Bi/GO nanohybrid exhibits a remarkably enhanced photocurrent density in comparison with the bare Bi sphere, suggesting the more efficient charge separation of Bi/GO sample due to the assistance of GO. In addition, EIS measurements were carried out to further investigate the charge transfer resistance and separation efficiency of the charge carriers in Fig. 11b, and the results showed that the Bi/GO nanohybrid presents a smaller arc radius than bare Bi sphere, once again indicating the high efficiency of charge transfer and separation of Bi/GO.

A mechanism for the enhanced photocatalytic activity over Bi/GO nanohybrids is depicted as follows (Fig. 12). The resonance energy of Bi spheres usually occurs in the UV light. The interaction between the resonant photons and the surface electrons results in a high absorption coefficient of photons in resonance with plasmon excitation and capacitive coupling between clusters of plasmonic Bi spheres. When the Bi spheres are irradiated with 280 nm UV light, the collective oscillation of electrons on the Bi spheres is induced by the incident light because of the SPR effect. A strong electric field and a high concentration of energetic electrons are then formed or produced at the Bi spheres surface. Graphene oxide, adjacent to the Bi spheres, could act as an acceptor of the photogenerated electrons from Bi and ensure fast charge transportation via its extended π -conjugation conductivity structure, and therefore, an effective charge-hole separation and admirable photocatalytic activity can be achieved [41,42]. Besides, the GO sheets can enhance NO adsorption and photocatalytic activity due to the increased

pollutant concentration in the reaction sites. Moreover, compared with the pure Bi spheres, the Bi spheres in the Bi/GO nanohybrid yield strong electromagnetic field to promote charge transfer because of the small diameter. Then the energetic electrons gain enough energy under UV irradiation to activate reactant molecules adsorbed on the composite and induce chemical reactions. Those electrons may react with oxygen to produce $\cdot O_2^-$ species, and holes on Bi can oxidize H_2O to generate $\cdot OH$, which are involved in removal of NO pollutant. The related reactions are shown in Eqs. (2)–(7).



4. Conclusion

In summary, we report a simple one-step solvothermal method to synthesize Bi spheres/graphene oxide nanohybrids. The optical responses and the absorption efficiency of Bi nanosphere with different sizes are simulated to confirm the SPR absorption based on Mie theory and FIT code. The local electromagnetic field arising from the SPR effects of Bi spheres was also simulated with a rigorous Maxwell's solver. These results provide theoretical support for development of rhombohedral Bi as a direct plasmonic photocatalyst. Bi/GO nanohybrid exhibited admirable and stable photocatalytic activity towards removal of NO under 280 nm light irradiation, mainly resulting from the promotion effects of GO in electron transfer and NO adsorption. The related growth and plasmonic photocatalytic mechanisms of Bi/GO composite system were proposed. This work provides new insights into the design of non-noble metal based plasmonic photocatalysts with efficient activity.

Acknowledgements

This research is financially supported by the National Natural Science Foundation of China (21501016, 51478070 and 51108487), the National Key R&D project of China (2016YFC0204702), the Innovative Research Team of Chongqing (CXTDG201602014), the Natural Science Foundation of Chongqing (cstc2016jcyjA0481), and

the Science and Technology project of Chongqing Education Commission (KJ1600625).

Appendix A. Supplementary data

Supplementary data associated with this article can be found, in the online version, at <http://dx.doi.org/10.1016/j.apcatb.2017.05.040>.

References

- [1] D.R. Dreyer, S. Park, C.W. Bielawski, R.S. Ruoff, *Chem. Soc. Rev.* 39 (2010) 228–240.
- [2] X. Jiang, J. Nisar, B. Pathak, J. Zhao, R. Ahuja, *J. Catal.* 299 (2013) 204–209.
- [3] V. Chandra, J. Park, Y. Chun, J.W. Lee, I.-C. Hwang, K.S. Kim, *ACS Nano* 4 (2010) 3979–3986.
- [4] L.T. Duy, T.Q. Trung, V.Q. Dang, B.U. Hwang, S. Siddiqui, I.Y. Son, S.K. Yoon, D.J. Chung, N.E. Lee, *Adv. Funct. Mater.* 26 (2016) 4329–4338.
- [5] F. Li, X. Jiang, J. Zhao, S. Zhang, *Nano Energy* 16 (2015) 488–515.
- [6] R. Vinoth, P. Karthik, C. Muthamizhchelvan, B. Neppolian, M. Ashokkumar, *Phys. Chem. Chem. Phys.* 18 (2016) 5179–5191.
- [7] F. Perreault, A.F. De Faria, M. Elimelech, *Chem. Soc. Rev.* 44 (2015) 5861–5896.
- [8] D. Chen, L. Zou, S. Li, F. Zheng, *Sci. Rep.* 6 (2016).
- [9] Y. Zhou, Q. Yi, M. Xing, L. Shang, T. Zhang, J. Zhang, *Chem. Commun.* 52 (2016) 1689–1692.
- [10] R. Verma, S.K. Samdarshi, *J. Phys. Chem. C* 120 (2016) 22281–22290.
- [11] S.K. Kim, H. Kim, H. Chang, B.-G. Cho, J. Huang, H. Yoo, H. Kim, H.D. Jang, *Sci. Rep.* 6 (2016).
- [12] B. Qiu, Q. Li, B. Shen, M. Xing, J. Zhang, *Appl. Catal. B: Environ.* 183 (2016) 216–223.
- [13] S. Sarina, E.R. Waclawik, H. Zhu, *Green Chem.* 15 (2013) 1814–1833.
- [14] Y.-L. Cui, X.-N. Guo, Y.-Y. Wang, X.-Y. Guo, *Sci. Rep.* 5 (2015).
- [15] T. Bora, D. Zoepfl, J. Dutta, *Sci. Rep.* 6 (2016).
- [16] F. Dong, T. Xiong, Y. Sun, Z. Zhao, Y. Zhou, X. Feng, Z. Wu, *Chem. Commun.* 50 (2014) 10386–10389.
- [17] F. Dong, Q. Li, Y. Sun, W.-K. Ho, *ACS Catal.* 4 (2014) 4341–4350.
- [18] F. Dong, Z. Zhao, Y. Sun, Y. Zhang, S. Yan, Z. Wu, *Environ. Sci. Technol.* 49 (2015) 12432–12440.
- [19] G. Jiang, X. Li, M. Lan, T. Shen, X. Lv, F. Dong, S. Zhang, *Appl. Catal. B: Environ.* (2017).
- [20] R. Fu, S. Xu, Y.-N. Lu, J.-J. Zhu, *Cryst. Growth Des.* 5 (2005) 1379–1385.
- [21] S. Cao, P. Zhou, J. Yu, *Chin. J. Catal.* 35 (2014) 989–1007.
- [22] S. Sun, W. Wang, *RSC Adv.* 4 (2014) 47136–47152.
- [23] L. Ye, Y. Su, X. Jin, H. Xie, C. Zhang, *Environ. Sci. Nano* 1 (2014) 90–112.
- [24] N. Zhang, R. Ciriminna, M. Pagliaro, Y.-J. Xu, *Chem. Soc. Rev.* 43 (2014) 5276–5287.
- [25] Z. Ni, Y. Sun, Y. Zhang, F. Dong, *Appl. Surf. Sci.* 365 (2016) 314–335.
- [26] N. Zhang, D. Chen, F. Niu, S. Wang, L. Qin, Y. Huang, *Sci. Rep.* 6 (2016).
- [27] F. Dong, Y. Sun, M. Fu, Z. Wu, S. Lee, *J. Hazard. Mater.* 219 (2012) 26–34.
- [28] J. Wang, F.E. Osterloh, *J. Mater. Chem. A* 2 (2014) 9405–9411.
- [29] D. Zhou, H. Yang, Y. Tu, Y. Tian, Y. Cai, Z. Hu, X. Zhu, *Nanoscale Res. Lett.* 11 (2016) 1–8.
- [30] T. Wieland, *Electronics and Communications AEU* 31, 1977, pp. 116–120.
- [31] C. Pflaum, Z. Rahimi, *Numer. Linear Algebra* 18 (2011) 653–670.
- [32] S. Yan, J. Krantz, K. Forberich, C. Pflaum, C.J. Brabec, *J. Appl. Phys.* 113 (2013) 154303.
- [33] H.-J. Hagemann, W. Gudat, C. Kunz, Optical Constants from the Far Infrared to the X-Ray Region: Mg, Al, Cu, Ag, Au, Bi, C, and Al₂O₃. Report SR-74/7. Deutsches Elektronen-Synchrotron: Hamburg, (1974).
- [34] M. Long, Y. Qin, C. Chen, X. Guo, B. Tan, W. Cai, *J. Phys. Chem. C* 117 (2013) 16734–16741.
- [35] H. Ma, Y. Jiao, B. Yin, S. Wang, S. Zhao, S. Huang, W. Pan, S. Chen, F. Meng, *Chemphyschem* 5 (2004) 713–716.
- [36] R. Sharma, K.K. Kar, *Electrochim. Acta* 156 (2015) 199–206.
- [37] T. Xiong, F. Dong, Z. Wu, *RSC Adv.* 4 (2014) 56307–56312.
- [38] D. Wang, X. Li, J. Chen, X. Tao, *Chem. Eng. J.* 198 (2012) 547–554.
- [39] Y. Min, K. Zhang, W. Zhao, F. Zheng, Y. Chen, Y. Zhang, *Chem. Eng. J.* 193 (2012) 203–210.
- [40] Z. Zhao, W. Zhang, X. Lv, Y. Sun, F. Dong, Y. Zhang, *Environ. Sci. Nano* 3 (2016) 1306–1317.
- [41] S. Song, B. Cheng, N. Wu, A. Meng, S. Cao, J. Yu, *Appl. Catal. B: Environ.* 181 (2016) 71–78.
- [42] X. Zeng, Z. Wang, N. Meng, D.T. McCarthy, A. Deletic, J.-h. Pan, X. Zhang, *Appl. Catal. B: Environ.* 202 (2017) 33–41.